

Low-energy excitations of the semimetallic one-dimensional $S=1/2$ antiferromagnet Yb_4As_3

B. Schmidt, H. Aoki, T. Cichorek, J. Custers, Philipp Gegenwart, M. Kohgi, M. Lang, C. Langhammer, A. Ochiai, S. Paschen, F. Steglich, T. Suzuki, P. Thalmeier, B. Wand, A. Yaresko

Angaben zur Veröffentlichung / Publication details:

Schmidt, B., H. Aoki, T. Cichorek, J. Custers, Philipp Gegenwart, M. Kohgi, M. Lang, et al. 2001. "Low-energy excitations of the semimetallic one-dimensional $S=1/2$ antiferromagnet Yb_4As_3 ." *Physica B: Condensed Matter* 300 (1-4): 121-38.
[https://doi.org/10.1016/s0921-4526\(01\)00576-2](https://doi.org/10.1016/s0921-4526(01)00576-2).

Low-energy excitations of the semimetallic one-dimensional $S = 1/2$ antiferromagnet Yb_4As_3 [☆]

B. Schmidt^{a,*}, H. Aoki^a, T. Cichorek^a, J. Custers^a, P. Gegenwart^a, M. Kohgi^b, M. Lang^{a,c}, C. Langhammer^a, A. Ochiai^d, S. Paschen^a, F. Steglich^a, T. Suzuki^{a,e}, P. Thalmeier^a, B. Wand^a, A. Yaresko^a

^aMax Planck Institute for the Chemical Physics of Solids, Noethnitzer Str. 40, 01187 Dresden, Germany

^bDepartment of Physics, Tokyo Metropolitan University, Hachioji, Tokyo 192-0397, Japan

^cInstitute for Physics, University of Frankfurt, 60054 Frankfurt (Main), Germany

^dCenter for Low Temperature Science, Tohoku University, Sendai 980-8578, Japan

^eDepartment of Physics, Tohoku University, Sendai 980-8578, Japan

Abstract

We investigate a new route to quasi-one-dimensional spin-chain systems which originates from the charge-ordering transition out of a homogeneous mixed-valence state. We present evidence that Yb_4As_3 and P, Sb doped mixed crystals are well described by this mechanism. Many thermodynamic and low-temperature transport heavy-fermion-like properties can be explained by the existence of low-lying quasi-one-dimensional spin excitations in the Yb^{3+} -chains. The observation of soliton excitations in a transverse external field gives further support to the existence of spin chains in Yb_4As_3 . We also present recent results on spin-glass behavior at very low temperature caused by the interchain coupling and disorder. In addition, the yet unexplained magnetotransport effects are discussed.

Keywords: Low-energy excitations; Semimetals; Antiferromagnets; Yb_4As_3

1. Introduction

The study of one-dimensional spin systems is of great interest for the understanding of generic quantum many-body effects which have no classi-

cal counterparts. An example is the connection between long-range behavior of spin correlation functions and the low-lying spin excitations in one-dimensional Heisenberg antiferromagnetic chains. While for $S = 1$ a “Haldane gap” in the excitation spectrum exists, leading to an exponential decay of the spin correlations, spin chains with $S = \frac{1}{2}$ show the gapless two-spinon continuum excitations as described by des Cloizeaux and Pearson [1] which is connected with the quasi-long-range order characterized by an algebraic decay of the spin correlations at long distance. Perturbations

[☆]Dedicated to Professor Dr. Erwin Müller-Hartmann on the occasion of his 60th birthday.

*Corresponding author. Tel.: +49-351-4646-2235; fax: +49-351-4646-3232.

E-mail address: bs@cpfs.mpg.de (B. Schmidt).

like exchange anisotropies, interchain coupling, staggered fields caused by Dzyaloshinskii–Moriya interactions and alternating g -tensors as well as lattice dimerization can lead to a gap formation also for $S = \frac{1}{2}$ chains. In some cases the low-lying excitations in the continuum limit can be well described by a quantum sine-Gordon model which leads to localized soliton-like excitations in addition to the extended spinon excitations. Most observations of these fundamental properties of spin chains have so far been studied in insulating Cu oxides or halides ($S = \frac{1}{2}$) or Ni ($S = 1$) compounds where the spin chains are dictated by the crystal structure of the insulator at all temperatures.

Recently, an exciting new route to one-dimensional spin physics has been found in compounds that exhibit a charge-ordering transition. In such compounds no localized spins on fixed atomic positions exist at high temperatures. They rather are homogeneous mixed-valence (semi-)metals or valence-fluctuating insulators at high temperatures. Their 3d or 4f electrons are strongly correlated and close to localization, i.e., having a low effective kinetic energy. If the *intersite* Coulomb repulsion is large enough it may dominate the kinetic energy and, once the charge-disorder entropy due to hopping is low enough, lead to a charge-ordering transition at a critical temperature T_{co} below which the valence fluctuations are suppressed. The resulting inhomogeneous mixed-valence state consists of two species of ions with valence Z and $(Z + 1)$. This transition may be compared to a Wigner crystallization on a lattice [2], and its earliest example is the Verwey transition in magnetite [3], although this picture turned out to be too simplified for this compound.

If one of the valence species, say Z , has no magnetic moment, a fascinating possibility arises. The charge ordering transition may lead to a structure where the species $(Z + 1)$ with spin S occupies only sites which lie on well-isolated chains (not necessarily linear) with only weak exchange interactions between the chains, thus creating a one-dimensional system of localized atomic spins at low temperature out of the high-temperature state.

This new scenario has recently been found to be realized in the 3d-layer compound sodium vanadate [4] where in addition an exchange dimerization in the chains leads to a spin-gap formation. The best studied and well confirmed system for the charge-ordering route to one-dimensional spin physics is the 4f-pnictide compound Yb_4As_3 . It is the aim of this article to review the existing experimental and theoretical research to support this picture in detail.

Yb_4As_3 is a semimetallic pnictide compound which belongs to a whole family of R_4X_3 (R = rare earth, $\text{X} = \text{As}, \text{Bi}, \text{P}, \text{Sb}$) compounds which have anti- Th_3P_4 structure, see Table 1. They have first been systematically investigated by Ochiai et al. [5]. These mixed-valence compounds may both be insulating or (semi-)metallic depending on the number of holes present in the pnictide p -valence bands. The more metallic compounds stay in a homogeneous mixed-valence state for all temperatures investigated. If only a few hole carriers are present, the intersite Coulomb interactions between the R-ions will be badly screened and a charge ordering of the two ionic species R^{2+} and R^{3+} at a temperature T_{co} is observed. If one species has no magnetic moment, the other species of ions with nonzero moment will form a *single family of parallel antiferromagnetic spin chains*. This is the case for all compounds in Table 1 which have finite T_{co} , except for Eu_4As_3 , where the Eu^{2+} -ions carry the nonzero magnetic moment. If the magnetic interchain coupling is large enough, magnetic order will appear at low temperatures as, e.g., is the case in Sm_4Bi_3 with $T_C \approx 2.7$ K. On the other hand, for very weak interchain coupling one has a quasi-one-dimensional Heisenberg antiferromagnet down to very low temperatures. This unique case is realized in Yb_4As_3 and also presumably in Yb_4P_3 and the mixed systems. In contrast to this scenario, Eu_4As_3 forms a three-dimensional magnetic system, with the magnetic ordering temperature being substantially larger than in Sm_4Bi_3 .

This article is organized as follows. In Section 2, we discuss the charge-ordering transition and its description within a mean-field model. Section 3 investigates the crucial concept how one-dimensional spin physics, which dominates the low-temperature thermodynamics of Yb_4As_3 , emerges

Table 1
Compilation of the properties of R_4X_3 compounds^a

Composition	T_{co} (K)	T_C (K)	$J(R^{2+})$	$J(R^{3+})$	n^{3+}	a (Å)	n (f.u.) ⁻¹	γ (mJ/mol K ²)	Ref.
(Yb _{0.85} Lu _{0.15}) ₄ As ₃	—	—	—	—	—	8.786	—	100	[6]
Yb ₄ P ₃	330	—	0	7/2	—	8.564	—	250	[6]
Yb ₄ (As _{0.6} P _{0.4}) ₃	295	—	0	7/2	—	8.700	0	250	[7]
Yb ₄ (As _{0.7} P _{0.3}) ₃	290	—	0	7/2	—	8.720	—	—	[7]
Yb ₄ (As _{0.95} P _{0.05}) ₃	285	—	0	7/2	—	8.780	—	—	[8]
Yb ₄ As ₃	295	—	0	7/2	0.25	8.788	0.001	200	[5,9,10]
Yb ₄ (As _{0.94} Sb _{0.06}) ₃	260	—	0	7/2	—	8.823	—	—	[8]
Yb ₄ (As _{0.88} Sb _{0.12}) ₃	231	—	0	7/2	—	8.851	0.004	220	[11]
Yb ₄ (As _{0.76} Sb _{0.24}) ₃	110	—	0	7/2	—	8.916	—	200	[8]
Yb ₄ (As _{0.71} Sb _{0.29}) ₃	—	—	0	7/2	—	8.944	0.036	300	[12]
Yb ₄ (As _{0.36} Sb _{0.64}) ₃	—	—	0	7/2	—	9.128	—	220	[6]
Yb ₄ Sb ₃	—	—	0	7/2	0.34	9.322	0.567	40	[5,10,13]
Yb ₄ Bi ₃	—	—	0	7/2	0.10	9.573	0.395	10	[5,10,13]
Eu ₄ As ₃	340	18	7/2	0	0.25	9.176	—	—	[5,14]
Eu ₄ Bi ₃	—	—	7/2	0	(0)	10.00	—	—	[13]
Sm ₄ As ₃	—	160	0	5/2	(1)	8.822	—	50	[15,16]
Sm ₄ Sb ₃	—	160	0	5/2	(1)	9.300	—	—	[13,15]
Sm ₄ Bi ₃	260	2.7	0	5/2	0.30	9.814	0.011	0	[5,13,15,17]

^aSymbols used: T_{co} : charge-ordering transition temperature accompanied by a structural transition $\bar{I}43d \rightarrow R3c$, T_C : magnetic ordering transition temperature (ferromagnetic for all compounds except for Sm₄Bi₃, where the type of magnetic ordering is unknown), n^{3+} : number of trivalent R-ions per formula unit estimated from photoemission and/or Mössbauer spectroscopy (values in parentheses: estimated from the lattice constant), a : cubic lattice constant, except for Eu₄As₃: trigonal lattice constant, n : carrier concentration at low temperatures estimated from the inverse Hall coefficient, γ : linear specific-heat coefficient.

from the charge-ordering transition. In Section 4, we discuss the evidence for localized soliton-like spin excitations as obtained from the field dependence of the specific heat, thermal expansion and transport coefficients. This lends further support to the one-dimensional spin-chain picture of Yb₄As₃. In Section 5, we present recent results for the collective magnetic behavior, i.e., spin-glass freezing found at very low temperatures where the interchain coupling becomes important. In Section 6, we discuss recent results on transport properties, notably their field dependences, which are not understood so far, but are likely to be connected with the existence of light and heavy carriers found in the LSDA+U band-structure calculations. Section 7 finally gives our conclusion and outlook.

2. Charge-ordering transition

The high-temperature phase of Yb₄As₃ is cubic (lattice constant $a = 8.788$ Å) and has the anti-Th₃P₄ crystal structure with space group $\bar{I}43d$. The

Yb-ions occupy the phosphorus sites on the three-fold symmetry axes, the As-ions are located on the Thorium sites. The arrangement of the Yb-sites can be viewed as being aligned on four families of interpenetrating chains oriented parallel to the space diagonals of a cube, known as body-centered cubic rod packing [18] which is illustrated in Fig. 1.

Chemical-valence counting assuming that the As-ions are trivalent shows that three quarter of the Yb-ions have filled 4f shells with a valency 2+, and one quarter with valency 3+ has one hole in the f-shell (f^{13} -configuration). In the high-temperature phase, all Yb-sites are equivalent, and the holes in the f-shells are moving between the Yb-ions due to hybridization with the As-4p holes: the compound is in a metallic intermediate-valence state with an average valency of $2.25+$. Mössbauer spectroscopy data on ¹⁷⁰Yb give clear evidence that below 50 K the system contains about 20% Yb³⁺-ions characterized by a $4f^{13}$ -configuration and a $J = 7/2$ ground-state multiplet [9].

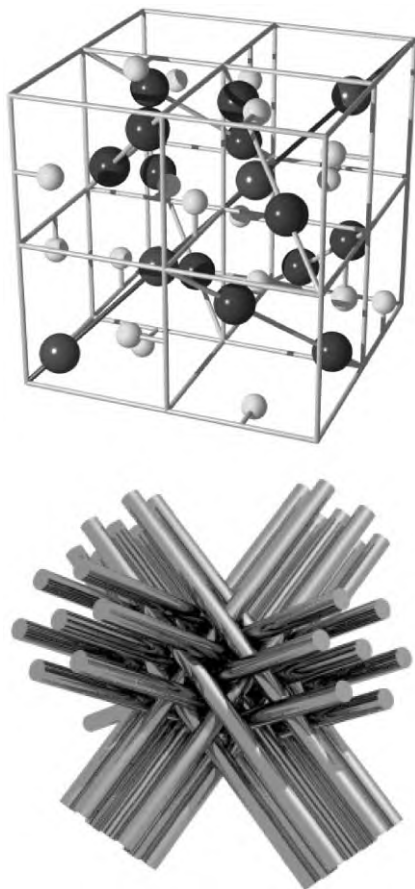


Fig. 1. Top: crystal structure of Yb_4As_3 in the cubic phase. Large balls denote the Yb-ions, small balls the As-ions. Bottom: the four families of chains formed by the Yb-ions of Yb_4As_3 , represented by four families of interpenetrating rods oriented parallel to the space diagonals of a cube.

At $T_{\text{co}} \approx 295$ K, a first-order structural phase transition has been observed which is accompanied by discontinuities of various quantities, e.g., the electrical resistivity and the Hall coefficient, see Figs. 2 and 3. At the structural transition, Yb_4As_3 shrinks along one of the four equivalent chain directions, in the following called the “short” chain [19]. This transition is approximately volume-conserving. The resulting trigonal unit cell has space group $R\bar{3}c$ with the short chain being parallel to the main axis. The trigonal angle is 90.8° [19,5].

Along with the transition to the trigonal phase, a charge ordering of the Yb-ions occurs. The 4f

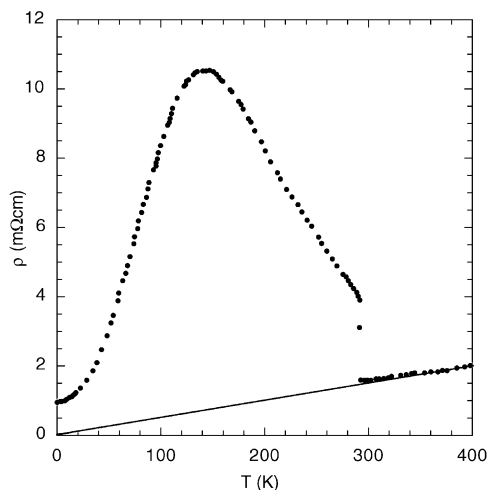


Fig. 2. Temperature dependence of the electrical resistivity of Yb_4As_3 . The jump at 295 K indicates the charge-ordering transition. The solid line extrapolates the linear T -dependence observed in the high-temperature phase [5].

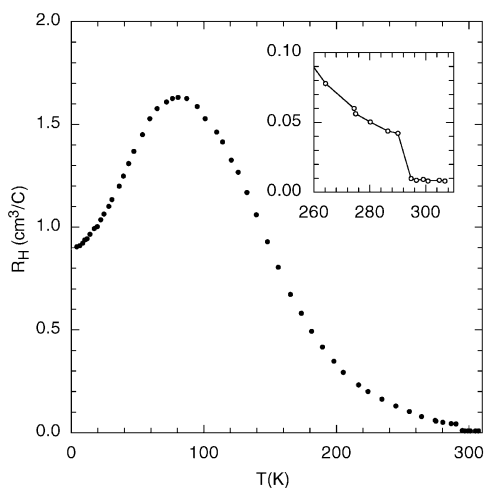


Fig. 3. Temperature dependence of the Hall coefficient of Yb_4As_3 . The insert shows the abrupt change at 295 K [5].

electronic state of Yb_4As_3 changes from a valence-fluctuating state in the cubic phase to a slightly incomplete charge-ordered state which can be expressed as $\text{Yb}^{3+}\text{Yb}_3^{2+}\text{As}_3^{3-}$, where the Yb^{3+} -ions are arranged predominantly on the short chain parallel to, e.g., the former cubic $\langle 111 \rangle$ direction. The low-temperature Hall coefficient R_H is positive, implying hole conduction and has a value

of $(eR_H)^{-1} = 7 \times 10^{18} \text{ cm}^{-3}$ [5]. Assuming the presence of only one type of charge carriers, their density is as small as approximately 0.001 per Yb^{3+} -ion.

The model to explain the transition is based on a band Jahn–Teller effect of correlated electrons (CBJT) [20]. The 56 Yb 4f-bands have an overall width of $\sim 0.2 \text{ eV}$ which arises from effective f–f hopping via hybridization with pnictide valence states [21]. To reduce the complexity of the f-bands the assumption is made that they can be described by four degenerate quasi-one-dimensional bands associated with the chains. The filling of each of these bands corresponds to the number of Yb-4f^{13} states in the chain associated with it.

Such a model is rather similar to the Labbé–Friedel model for 3d states in A15 compounds [23] where chains parallel to the cubic axes are the dominant structural elements. Although such models may not be literally true due to the three-dimensionality of the electronic states, they describe the important aspect that a strain coupling to the degenerate band states may easily lead to distortions of the cubic structure and simultaneous repopulation among the 4f states of Yb_4As_3 .

There is a strong deformation-potential coupling typical for intermediate-valence systems which removes this degeneracy by a trigonal CBJT-distortion. When the Jahn–Teller transition takes place, the crystal shrinks in the $\langle 111 \rangle$ -direction, lifting the four-fold degeneracy. The four equivalent chains are subdivided into one along the $\langle 111 \rangle$ -direction and the three remaining “long” chains. Since the Yb^{3+} -ions have a smaller radius than the Yb^{2+} -ions, it is natural to think of the CBJT transition as being related to the ordering of Yb^{3+} -ions along the space diagonal $\langle 111 \rangle$.

The CBJT transition is described by an effective Hamiltonian of the form

$$H = -t \sum_{\mu=1}^{\mu_f} \sum_{\langle ij \rangle \sigma} f_{i\mu\sigma}^\dagger f_{j\mu\sigma} + \varepsilon_\Gamma \sum_{\mu=1}^{\mu_f} \sum_{i\sigma} \Delta_\mu f_{i\mu\sigma}^\dagger f_{i\mu\sigma} + N_L \mu_f c_0 \varepsilon_\Gamma^2, \quad (1)$$

where μ labels the summation over the $\mu_f = 4$ different chains, and $\langle ij \rangle$ denotes the summation over nearest-neighbor sites along one chain. The $f_{i\mu\sigma}^\dagger$ create f-holes with spin σ at site i of chain μ . The bandwidth $4t = 0.2 \text{ eV}$ is chosen as obtained from LDA calculations [21] and an effective spin degeneracy of $2S + 1 = 2$ is used. The second term in Eq. (1) describes the volume-conserving coupling of the trigonal strain ε_Γ ($\Gamma \equiv \Gamma_5$) to the f-bands characterized by a deformation potential $\Delta_\mu = \Delta [\delta_{\mu 1} - (1 - \delta_{\mu 1})/(\mu_f - 1)]$. This deformation potential describes the effect of the nearest-neighbor Coulomb repulsion between the Yb-sites. (Note that the three nearest Yb-neighbors of an Yb-ion on one chain are located on chains belonging to the other three families.) Writing this interaction as an attractive nearest-neighbor Coulomb interaction within the chains with an energy gain $\propto V$, one has, after Hartree–Fock decoupling, the relations $\Delta^2/c_0 = 6V$ and $\Delta \varepsilon_\Gamma = -2V(n_{\mu=1} - 1/8)$. Here, c_0 is the background elastic constant for one chain. Changes of the bandwidths due to the distortion are small and can be neglected.

The third term in Eq. (1) is the elastic energy associated with the distortion. Here N_L is the number of sites in a chain and $c_0/\Omega = 10^{11} \text{ erg/cm}^3$ is chosen, where Ω denotes the volume of a unit cell. Note that the bulk elastic constant $c_\Gamma^0 = 4c_0$ which is close to the experimental value of $3.57 \times 10^{11} \text{ erg/cm}^3$ [22].

The Hamiltonian (1) does not yet contain the strong intra-ionic Coulomb interactions between the holes at the Yb-sites. Therefore, it is applicable only above T_{co} , where the number of holes per Yb-site is $1/4$ and somewhat below T_{co} . At low temperatures, the Coulomb interactions and the strong correlations which they imply are crucial (see below). However, for modeling the CBJT phase transition the Hamiltonian (1) is sufficient. The condition for a phase transition to occur is $\Delta^2/(4tc_0) > 3$. In Ref. [20] $\Delta = 5 \text{ eV}$ was chosen, which corresponds to a reasonable Grüneisen parameter $\Omega \equiv \Delta/(4t) = 25$. From this, a transition temperature of $T_{\text{co}} \simeq 250 \text{ K}$ is obtained which is close to the observed $T_{\text{co}}^{\text{exp}} \simeq 295 \text{ K}$. The approach to the phase transition is signified by a strong softening of the trigonal-symmetry elastic constant c_{44} [22].

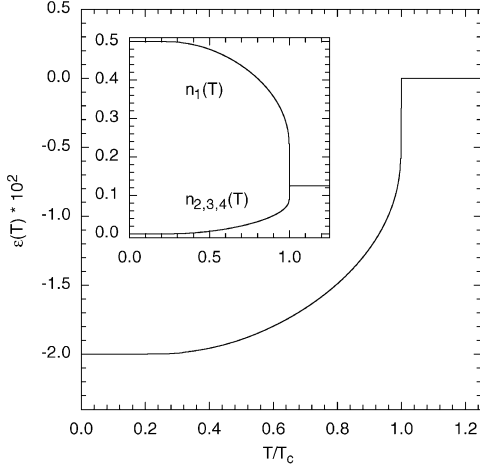


Fig. 4. Temperature dependence of the strain order parameter $\varepsilon_T(T)$. Inset: occupation numbers $n_\mu(T)$ of the four f-bands [20].

Below the phase-transition temperature, one obtains a trigonal strain-order parameter $\varepsilon_T(T)$ whose temperature variation, together with the band occupation $n_\mu(T)$, is shown in Fig. 4. At T_{co} , the four degenerate bands split with an associated shift of holes from the upper three-fold degenerate bands into the lower fourth band. The energy difference between the respective band centers is $\frac{4}{3}|\varepsilon_T \Delta|$. The equilibrium strain at low temperature is $\varepsilon_T = -\Delta/(8c_0) \simeq -0.02$. The increase in the hole occupation number of the lower band shows a similar behavior as $|\varepsilon_T(T)|$ until, at low T , the upper bands are empty (of holes) while the lower band is becoming half-filled. Note that in this model, charge ordering on chains and the band Jahn–Teller effect are completely equivalent pictures.

The particular ordering of the Yb^{3+} -ions described here was confirmed clearly by perturbed angular-correlation (PAC) measurements [24]. A direct proof for the charge ordering in Yb_4As_3 was given by polarized-neutron scattering [25,26]. The stabilization of the Yb^{3+} states on the short chains was further supported by temperature-dependent spectral changes in high-resolution photoemission spectroscopy [27]. A recent resonant X-ray diffraction experiment on the Yb L_3 -absorption edge gave an additional direct evidence for the particular one-dimensional charge order described here [28].

3. Low-temperature thermodynamic and transport properties at $B=0$: magnons

For $B=0$ and at temperatures below about 10 K, the thermodynamic properties of Yb_4As_3 resemble that of a typical heavy-fermion metal. Above $T \approx 0.5$ K, the specific heat is dominated by a term linear in temperature, $C = \gamma T$, with $\gamma \approx 200$ mJ/(K² mol) [29], cf. Fig. 5. Upon lowering the temperature, $C(T)/T$ shows a steep increase with a low-temperature asymptotic T^{-3} dependence and a shoulder-like anomaly near $T = 0.2$ K. We shall return to these low- T results in Section 5. The static magnetic susceptibility is almost T -independent between 10 and 2 K and extrapolates for $T \rightarrow 0$ to a rather large value of $\chi(T \rightarrow 0) \approx 3 \times 10^{-2}$ emu/mol. The Sommerfeld–Wilson ratio $R = \pi^2 k_B^2 \chi(T \rightarrow 0)/(3\mu_{\text{eff}}^2 \gamma)$ is of the order of unity. For very low temperatures, however, $\chi(T)$ like $C(T)/T$ shows a strong increase with decreasing temperature.

For $4 \text{ K} < T < 100 \text{ K}$, the electrical resistivity of Yb_4As_3 exhibits a temperature dependence that can be described well by $\rho(T) = \rho_0 + AT^2$, with a strongly enhanced A -coefficient, cf. Fig. 2. One usually would expect this behavior for metals with an enhanced density of states for low-energy fermionic charge degrees of freedom. In contrast

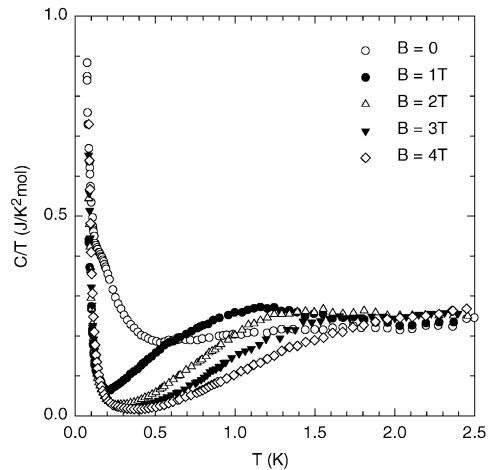


Fig. 5. Temperature dependence of the specific heat of a polydomain single-crystalline Yb_4As_3 sample in an applied magnetic field, shown as C/T vs. T [30,31].

to these, Yb_4As_3 has, according to the extremely large value of the Hall coefficient (cf. Fig. 3), almost no charge carriers, implying that the standard Kondo picture for the origin of these low-energy excitations of “heavy-fermion” metals cannot be applied. Instead, the low-temperature thermodynamics of Yb_4As_3 can be understood within the framework of the model introduced in the preceding section as follows:

As the short chain is approaching half-filling, the strong on-site Coulomb interaction in this chain must be taken into account. This is incorporated by an on-site Hubbard term with $U \sim 10$ eV which can be eliminated by making a canonical transformation onto a t - J -like Hamiltonian acting on states with no Yb^{2+} -sites in the short chain. Introducing an auxiliary boson b_i^\dagger to parameterize this constraint [32,33], the Hamiltonian in k -space, after a mean-field approximation, reads

$$H_{\text{MF}} = \sum_{\mu\nu} \sum_{k\sigma} E_{\mu\nu}(k) f_{k\mu\sigma}^\dagger f_{k\nu\sigma} + H_{\text{const}}, \quad (2)$$

$$E_{\mu\nu}(k) = \delta_{\mu\nu} \varepsilon_\mu(k) + r V_{\mu\nu}, \quad (3)$$

with $\varepsilon_1(k) = (r^2 + J\eta/t)\varepsilon(k) + \lambda + E_0$, $\varepsilon_{\mu>1}(k) = \varepsilon(k) \equiv -2t \cos(k)$, and $H_{\text{const}} = N_{\text{L}}(J\eta^2 - \lambda(1 - r^2))$. The mean-field approximation consists of the replacement $\langle b_i^\dagger \rangle \rightarrow r$ and of a saddle-point approximation to the Hubbard–Stratonovič field $\langle \sum_\sigma f_{i1\sigma}^\dagger f_{j1\sigma} \rangle \rightarrow \eta$. Here λ is an average Lagrange multiplier enforcing the above-mentioned constraint. The remaining parameters are $J = 4t^2/U$, and E_0 being the band-center of mass distance of the lower and upper bands due to the distortion. The matrix $V_{\mu\nu} = V(\delta_{\mu 1} + \delta_{\nu 1})(1 - \delta_{\mu\nu})$ serves for the coupling between the short chain and the other three.

For low temperatures, the thermodynamics of this effective Hamiltonian is essentially governed by a renormalization of the quasi-particle mass in the lower band,

$$\frac{m^*}{m_{\text{b}}} = \frac{t}{\delta t + \eta J} \simeq 100, \quad \eta = \mathcal{O}(1), \quad (4)$$

where m_{b} is the bare band mass of the Hamiltonian (1), and δ denotes the deviation of the filling of the short chains from one hole per site.

For $\delta \ll 1$, as it is the case for Yb_4As_3 , the effective mass for the low-energy excitations responsible for the very large specific heat is determined almost exclusively by the magnetic exchange energy J . These excitations correspond to the magnetic excitations (“magnons”) of an antiferromagnetic quasi-one-dimensional “ $S = \frac{1}{2}$ ” Heisenberg chain, where S is the pseudo-spin describing the lowest Kramers doublet of Yb^{3+} , slightly modified by the presence of $\delta \approx 0.001$ holes per Yb^{3+} -ion. This leads naturally to an enhanced linear specific heat for $k_{\text{B}}T/J \ll 1$ as, in fact, is observed (cf. Fig. 5).

Thermal and transport measurements on P- and Sb-doped samples gave further experimental evidence for the scenario described here [7,12,30] (Fig. 6): With increasing concentration x of phosphorus, the electrical resistivity of $\text{Yb}_4(\text{As}_{1-x}\text{P}_x)_3$ grows drastically, and with $x = 0.3$ it is nearly insulating, while the specific heat and the magnetic susceptibility are almost the same as those of pure Yb_4As_3 . With increasing Sb content x , the absolute value of the resistivity of $\text{Yb}_4(\text{As}_{1-x}\text{Sb}_x)_3$ decreases due to the increase of the number of charge carriers and the system becomes more metallic while again the specific-heat γ value is roughly the same as in the pure compound and thus almost independent of the carrier concentration. However, at 29% Sb-doping, the charge ordering seems to disappear, i.e., no discontinuity in thermodynamic and transport properties could be observed.

The crossover to the low- T spin-chain structure was well confirmed by inelastic-neutron scattering experiments by Kohgi et al. [25,34], see Fig. 7. They show that the low-temperature magnetic excitations in Yb_4As_3 are indeed very well described by the one-dimensional spin-excitation spectrum $\omega(q) = (\pi/2) \sin(aq)$ as described by des Cloizeaux and Pearson [1] where q is the wave number in $\langle 111 \rangle$ -direction and a the distance between the Yb^{3+} -ions along the short chains. More precisely, this dispersion describes the lower boundary of the two-spinon continuum, i.e., a continuum of spin excitations whose spectral function for a fixed momentum q diverges at this lower boundary [35,36]. From the maximum observed spin excitation energy of 3.8 meV $\approx k_{\text{B}}$.

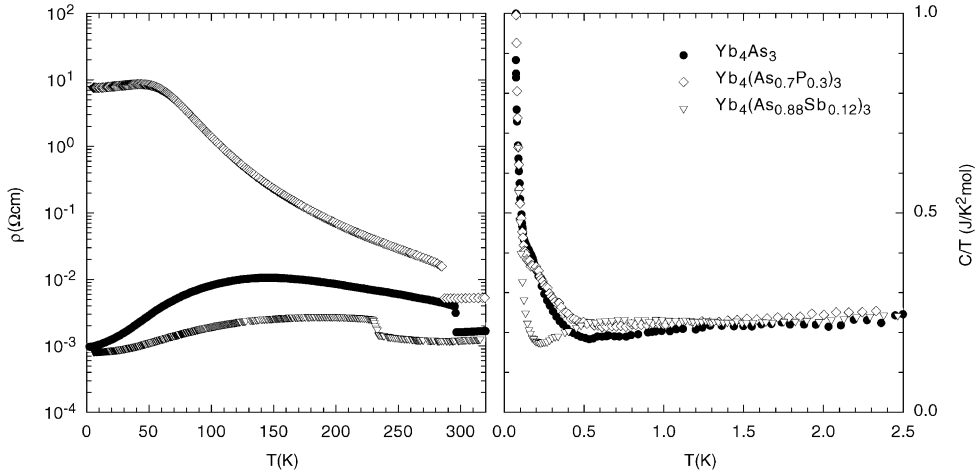


Fig. 6. Temperature dependence of the electrical resistivity (left) and the low-temperature specific heat divided by temperature (right) of Yb_4As_3 (bullets), $\text{Yb}_4(\text{As}_{0.7}\text{P}_{0.3})_3$ (diamonds), and $\text{Yb}_4(\text{As}_{0.88}\text{Sb}_{0.12})_3$ (triangles). Note the logarithmic ordinate for the resistivity plot.

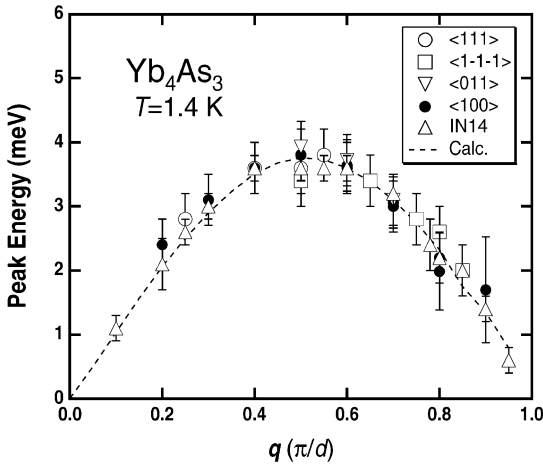


Fig. 7. Dispersion relation of the inelastic neutron-scattering peaks of Yb_4As_3 along the $\langle 111 \rangle$ -direction. The dashed curve represents the relation $\omega(q) = (\pi/2)J \sin(aq)$ [34].

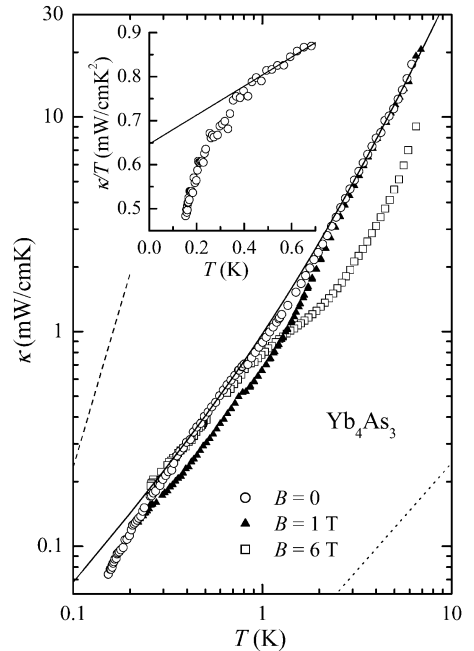


Fig. 8. Thermal conductivity κ vs. temperature T for Yb_4As_3 , in zero magnetic field and at 1 and 6 T. The meaning of the different lines is explained in the text. The inset shows the deviation of the data from the $aT + bT^2$ dependence at temperatures somewhat below 0.5 K.

40 K at $q = \pi/(2a)$ one obtains $J \approx k_B \cdot 25$ K in good agreement with the energy scale $k_B T^*$ estimated from the value of the specific-heat coefficient as measured.

In the following we discuss the thermal conductivity $\kappa(T)$ of a polydomain single-crystalline sample of Yb_4As_3 . Its temperature dependence is shown in Fig. 8 on a double-logarithmic scale, in zero magnetic field and at $B = 1$ T and

$B = 6$ T. The zero-field data may, between 0.4 and 6 K, be well approximated by $aT + bT^2$, with

$a = 0.65 \text{ mW/cm K}^2$ and $b = 0.33 \text{ mW/cm K}^3$ (cf. solid curve in Fig. 8 and its inset). We use some estimates to determine the mechanism responsible for this temperature dependence. The electronic contribution to the thermal conductivity calculated, with the help of the Wiedemann–Franz law, from the residual resistivity $\rho_0 \approx 1 \text{ m}\Omega \text{ cm}$ is more than one order of magnitude smaller than the measured $\kappa(T)$ (cf. dotted line in Fig. 8), suggesting that the experimentally observed linear-in- T term is not due to an electronic thermal conductivity. Owing to the small Wiedemann–Franz contribution it is also improbable that electrons are important scatterers for the phonons.

The phonon contribution can be estimated from the gas kinetic equation $\kappa = 1/3 \times C v A$, taking $C = 3 \text{ mJ/mol K}^4 \times T^3$ for the phonon specific heat and $v = 2975 \text{ m/s}$ for the sound velocity [37]. If boundary scattering from the smallest sample dimension of approximately $800 \mu\text{m}$ determined the mean free path A , much higher $\kappa(T)$ values should be observed (cf. dashed line in Fig. 8). Thus, the phonons appear to be subject to an additional scattering mechanism.

We propose that magnons play an important role in the thermal conductivity of Yb_4As_3 . They act both as heat carriers at the lowest temperatures (aT term) and as scatterers for the phonons at higher temperatures (bT^2 term). Applying the gas kinetic equation to magnon thermal conductivity with the above-mentioned magnon specific heat $C \approx 200 \text{ mJ}/(\text{K}^2 \text{ mol}) \times T$ and the magnon velocity $v = 2020 \text{ m/s}$ [34], our fit yields a magnon mean free path $A = 500 \text{ \AA}$, corresponding to 130 times the Yb^{3+} – Yb^{3+} distance. This mean free path, which is much smaller than the domain size of approximately $1 \mu\text{m}$ [16], is most probably due to scattering from static point defects on the Yb^{3+} chains. Due to the finite homogeneity range of Yb_4As_3 , Yb (and also As) vacancies at concentrations of up to several percent per formula unit are expected in single-phase samples [38], in agreement with our findings.

Two observations provide additional evidence for our interpretation of $\kappa(T)$. Firstly, the thermal conductivity drops below the $aT + bT^2$ law at temperatures somewhat below 0.5 K (cf. inset of Fig. 8), in agreement with the deviation from the

magnon-related γT term in the specific heat (Fig. 5) due to the spin-glass freezing. Secondly, the observed magnetic-field dependence is plausible within this interpretation. At $B = 1 \text{ T}$, the magnon thermal conductivity is reduced, but the reduction of the phonon–magnon scattering rate reinforces the phonon conductivity and, thus, overcompensates this effect in higher fields such that, at $B = 6 \text{ T}$, the zero-field thermal conductivity is almost recovered. We shall address the broad minimum in $\kappa(T)$, found when a magnetic field is applied, in the subsequent section.

4. Field-induced spin gap and solitons

In the following we discuss the response of the $S = \frac{1}{2}$ spin chains to external magnetic fields. Concerning the dependence of the specific-heat coefficient γ for an antiferromagnetic $S = \frac{1}{2}$ Heisenberg chain on an applied magnetic field B , one would expect deviations from $\gamma(B = 0)$ of the order $(B/J)^2$, i.e. about 1% at 4 T uniformly for all temperatures with $k_B T/J \ll 1$. As is demonstrated in Fig. 5, the behavior of the specific heat is quite different.

Above 2 K changes in γ are indeed comparatively small. At lower temperatures, however, its field dependence is dramatic. Upon increasing the field, $C(T)/T$ becomes progressively reduced slightly above the temperature at which the low- T upturn sets in, while at somewhat higher temperatures a broad hump forms which is continuously shifted towards higher T . After subtracting a T^{-3} term from $C(T)/T$ due to nuclear contributions, the data are found to level off below $T \approx 0.2 \text{ K}$ at a constant value $\gamma(B)$ [30,31]. Already at 4 T , $\gamma(B)$ is strongly suppressed, indicating that an additional energy scale much smaller than J ($k_B \cdot 25 \text{ K}$) should exist.

This observation can be incorporated by introducing a small interchain-coupling J' between adjacent parallel short chains, leading immediately to a field-dependent excitation gap $\Delta \sim \sqrt{|JJ'|}$ and hence to a field dependence of the thermodynamic quantities like the specific heat [39]. In Fig. 9, the corresponding field dependence of the γ -coefficient is shown together with the experimental $\gamma(B)$

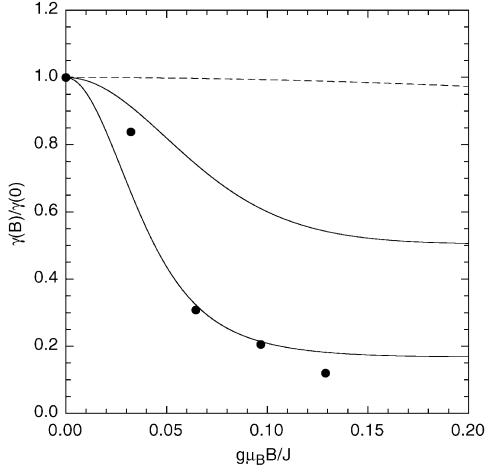


Fig. 9. Magnetic-field dependence of the γ -coefficient for the trigonal-chain structure. Bottom solid line: field applied perpendicular to the $\langle 111 \rangle$ direction, top solid line: field applied parallel to the $\langle 111 \rangle$ direction, both at $T \approx 0.5$ K. Dashed line: field dependence at $T \approx 5$ K. A ratio $J'/J = 10^{-4}$ was used [39]. The filled circles denote the data for Yb_4As_3 [30,31].

values. As long as $k_B T \gg \Delta$, this field dependence is insignificant, see the dashed line. Upon lowering the temperature to values around Δ , a strong field dependence in the range $|J'| \ll T \leq \Delta$ is observed, most pronounced for a transverse field direction. The validity of this approach is restricted to $|J'| \ll T$ due to the “three-dimensionality” of the crystal introduced by the interchain coupling at very low temperatures. For the size of magnetic fields considered here, the sign of J' is unimportant.

An alternative mechanism leading to the opening of a gap in the magnon-excitation spectrum was discussed by Uimin et al. [40]. They assigned the additional small energy scale to an intrachain dipolar interaction, which also results in a spin gap in an applied transverse magnetic field.

A field-induced opening of a gap in the excitation spectrum has been also observed for the quasi-one-dimensional system Cu benzoate [41], and a staggered field perpendicular to the $S = \frac{1}{2}$ chains was proposed [42] as the driving force for the gap opening in this case. In an external transverse field, both an alternating g tensor and

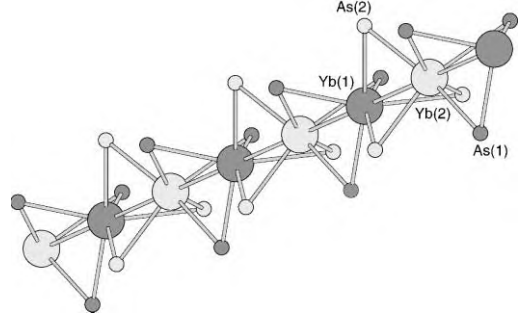


Fig. 10. Arrangement of the Yb^{3+} -ions along a short chain of Yb_4As_3 . The distance $\text{Yb}(1)\text{--As}(1)$ is smaller than the distance $\text{Yb}(1)\text{--As}(2)$ [8].

the Dzyaloshinskii–Moriya (DM) interaction may account for this staggered field.

In the case of Yb_4As_3 , if one takes into account the presence of the As atoms, cf. Fig. 10, one finds the following situation [43,44]. The local C_3 symmetry at the Yb sites on the short chains, and the absence of a center of inversion symmetry between two adjacent Yb^{3+} -ions allow for a uniaxial anisotropy in the symmetric part of the spin exchange as well as for the presence of an additional antisymmetric DM spin exchange interaction. The glide reflection with the glide vector parallel to the Yb^{3+} -chains requires an alternating sign for this antisymmetric part, if present. The same symmetry constraints apply to the g -tensor. The most general form of the Hamiltonian describing the low-energy magnetic degrees of freedom with an effective spin 1/2 therefore is given by

$$H = \sum_i J(i) S_i S_{i+1} + g(i) B S_i, \quad (5)$$

where the matrix $J(i)$ has the form

$$J(i) = \begin{pmatrix} J_{\perp} & (-)^i D & 0 \\ -(-)^i D & J_{\perp} & 0 \\ 0 & 0 & J_{\parallel} \end{pmatrix}, \quad (6)$$

and $g(i)$ correspondingly.

A detailed investigation of the wavefunctions for the $J = 7/2$ multiplet given by Shiba et al. [44] uncovered a hidden isotropy of the effective Hamiltonian above. The parameters J_{\parallel} , J_{\perp} , and D are not independent from each other. In fact,

there is only one energy scale $J \equiv J_{\parallel}$, and one has the relations $J_{\perp} = J \cos(2\theta)$, $D = J \sin(2\theta)$ with the phase angle θ to be determined experimentally. Additionally, they showed that the g -tensor is axially symmetric around the short chains and does not contain any antisymmetric part.

An alternating rotation of the local coordinate system around the chain direction by an angle $\pm\theta$ eliminates the DM interaction in $J(i)$: At *zero field*, the effective Hamiltonian is equivalent to the one-dimensional *isotropic* $S = \frac{1}{2}$ Heisenberg antiferromagnet. In addition, the uniform magnetic-field component perpendicular to the short chains induces a staggered field which reads

$$b = g_{\perp} \sin(\theta) n \times B, \quad (7)$$

where n is a unit vector pointing in the chain direction.

A low-energy effective-field theory of the Heisenberg model is given by the quantum sine-Gordon (SG) model with a Lagrangian density

$$\mathcal{L} = \frac{1}{2}((\partial_t \phi)^2 - v_{\text{SW}}^2 (\partial_x \phi)^2) - bC \cos(\beta \phi). \quad (8)$$

Here, ϕ is a boson field, v_{SW} is the spin-wave velocity, C is a constant, and b is the projection of the externally applied field onto the plane perpendicular to the chain in Yb_4As_3 . According to Refs. [42,43], the staggered field induces an excitation gap

$$\Delta \propto J^{1/3} b^{2/3}. \quad (9)$$

The quantum SG model was originally used to explain the opening of the spin gap clearly seen in Cu-benzoate when measured in a field of 3.5 T, applied perpendicularly to the Cu^{2+} chains [41]. However, the quantum SG model is a continuum approximation valid only for temperatures T appreciably lower than J . Its validity at elevated temperatures where field-induced humps occur in both Cu-benzoate [41] and Yb_4As_3 (Figs. 5 and 11a) has yet to be demonstrated.

These specific-heat maxima have their correspondence in even more pronounced peaks in the coefficient of the thermal expansion, $\alpha(T, B)$, (Fig. 11b). Since there are four equivalent cubic space diagonals at $T > T_{\text{co}}$, the samples exhibit a polydomain structure in the charge-ordered state. Monodomain crystals are obtained if a uniaxial

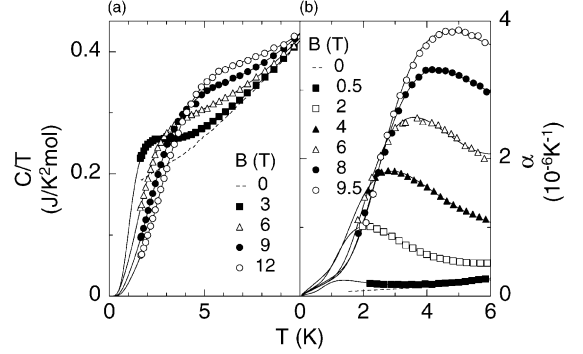


Fig. 11. Specific heat $C(T)/T$ (a) and thermal expansion $\alpha(T)$ (b) of Yb_4As_3 at varying magnetic fields. Solid lines are fits using a classical model, including both magnons and solitons [45,47].

pressure of the order of 100 bar is applied parallel to one of the four cubic space diagonals prior to cooling well below T_{co} . In our thermal-expansion measurement we can also apply uniaxial pressures (1–10 bar) along the measuring direction. In this way the polydomain structure can be varied deliberately. A detailed quantitative analysis of the field-induced peaks in $\alpha(T, B)$ for samples with different domain structures revealed unequivocally that a *finite* field component perpendicular to the short axis (i.e., the $S = \frac{1}{2}$ chains) is required to induce the anomaly [45]. Since this unique orientational dependence can neither be explained by the effect of the field on the extended magnon excitations nor by Schottky-type contributions (due to, e.g., isolated frozen magnetic moments on the long chains), the $C(T, B)$ and $\alpha(T, B)$ maxima displayed in Fig. 11 were ascribed [45] to localized soliton excitations. This appears natural, for they, too, require a finite field component perpendicular to the spin chains [46].

Because we want to investigate $\alpha(T, B)$ and the thermal conductivity $\kappa(T, B)$ in addition to $C(T, B)$, we use the classical SG solutions of a one-dimensional Heisenberg antiferromagnet with weak uniaxial anisotropy to fit our experimental data shown in Fig. 11. These solutions, usually called solitons, are described by their mass, m_s , and their rest energy, E_s . As discussed in Refs. [45,47], excellent fits are achieved if one allows for $m_s(B)$, $E_s(B)$, and a third adjustable parameter,

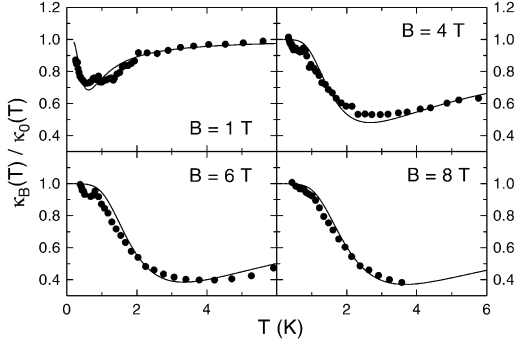


Fig. 12. Thermal conductivity of Yb_4As_3 at varying magnetic fields, $\kappa_B(T)$, normalized to the data at $B = 0$, $\kappa_0(T)$. Solid lines are fits for a resonant phonon-soliton scattering model [45].

i.e., the spin gap in the magnon spectrum, $\Delta(B)$, and a soliton-derived Grüneisen parameter, $\Gamma(B)$, in the case of $C(T, B)/T$ and $\alpha(T, B)$, respectively.

In the thermal conductivity $\kappa(B, T) \equiv \kappa_B(T)$ normalized to the zero-field data $\kappa_0(T)$, as discussed in Section 3, we find a flat minimum which becomes progressively deeper and shifted towards higher temperatures upon increasing the field (Fig. 12). The positions of these minima agree well with those of the $C(T, B)$ and $\alpha(T, B)$ maxima shown in Fig. 11. We, therefore, attribute the minima in κ_B/κ_0 vs. T to the scattering of the three-dimensional phonons by the magnetic solitons [45]. This scattering process was already held responsible previously [48] for similar observations in the $S = \frac{5}{2}$ spin-chain systems TMMC and DMMC. Here, a phonon-soliton resonance scattering was assumed, acting independently from the usual phonon-boundary scattering. Again, three fit parameters, $m_s(B)$, $E_s(B)$, and the relative strength of this resonance-scattering mechanism were used. Following Ref. [48], we can fit the experimental data of Fig. 12 reasonably well.

We can, therefore, state that our results of the specific heat, thermal expansion and thermal conductivity are well explained assuming solitary excitations for magnetic fields containing a non-zero component perpendicular to the spin chains. There exists a qualitative difference between the localized soliton and the extended magnon excitations concerning the thermal conductivity. Both types of excitations act as scattering centers for the dominant heat carriers, i.e., the phonons. In

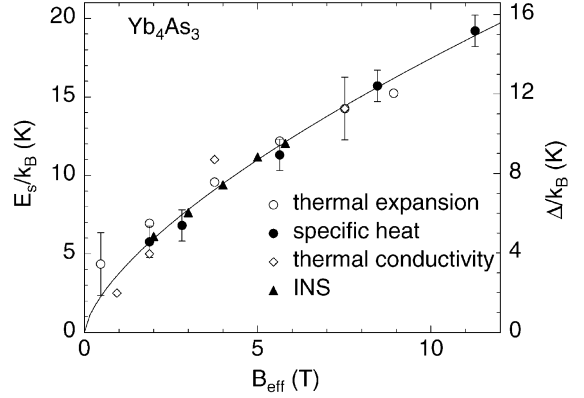


Fig. 13. Left ordinate: field dependence of the soliton rest energy E_s as derived from the fits in Figs. 11 and 12 with a transverse field component $B_{\text{eff}} = B \sin(70^\circ)$. Right ordinate: spin-excitation gap Δ as derived from inelastic neutron scattering (INS) [49]. The solid line is a fit $E_s(B) = \beta B_{\text{eff}}^{2/3}$ with $\beta = 3.74 \text{ K T}^{-2/3}$ [47] and $\Delta(B) = \beta' B_{\text{eff}}^{2/3}$ with $\beta' = 2.97 \text{ K T}^{-2/3}$, respectively.

contrast, only the magnons appear to act as heat carriers as well, as can be seen from the analysis of our thermal-conductivity measurements.

Naturally the application of the classical SG theory to quantum spin chains is strongly limited. In contrast to the prediction of the classical model where the *soliton rest energy* should be proportional to the field, our experimental results reveal $E_s \sim B^\nu$ with $\nu \approx 0.66$, see Fig. 13. This agrees with the field dependence of the *spin gap* obtained in the quantum SG model, cf. Eq. (9). We conclude that (1) solitons exist in antiferromagnetic quantum-spin chain systems and (2) in Yb_4As_3 , the spin gap, opening in the magnon spectrum, and the soliton rest energy are not independent of each other as they are in the classical model (cf. our above analysis of the $C(B, T)/T$ results), but they are identical, except for a constant prefactor: $\Delta(B) = \text{const.} \times E_s(B)$.

The presence of free carriers may change the exponent ν as shown in Ref. [58], where $\nu \sim 0.64$ was proposed to be more adequate. We would also like to note that recent neutron-scattering experiments [49,50] provide direct evidence for the field-induced gap opening in the spin excitation spectrum of Yb_4As_3 with a magnetic field applied perpendicular to the short-chain direction, see Fig. 13.

5. Ferromagnetic interchain coupling and spin-glass freezing

The anisotropy of the magnetic susceptibility of a single-domain Yb_4As_3 crystal was first measured by Aoki et al. from room temperature down to 2 K in a commercial SQUID magnetometer by applying uniaxial pressure along one of the $\langle 111 \rangle$ directions in an acrylic resin pressure cell [8,51], see Fig. 14. In this measurement, the single-domain formation was almost perfect since (1) with increasing uniaxial pressure a saturation of the pressure-induced anisotropy $\chi_{\parallel}(15\text{ K})/\chi_{\perp}(15\text{ K})$ was observed (χ_{\parallel} , χ_{\perp} denote the susceptibility along and perpendicular to the trigonal axis) and (2) the average susceptibility $\bar{\chi} = \chi_{\parallel}/3 + 2\chi_{\perp}/3$ coincided with that of the polydomain state (χ_m), studied without uniaxial pressure [8,51].

Above 7 K the T -dependence of χ_{\parallel} is well described by the sum of a constant van Vleck contribution and the uniform susceptibility of the $S = \frac{1}{2}$ antiferromagnetic Heisenberg chain [52] assuming an intrachain exchange coupling $J = 26\text{ K}$ [53] (see dotted line in Fig. 14). On the other hand, the huge upturn of χ_{\perp} is in accordance with the prediction of the staggered-field model which

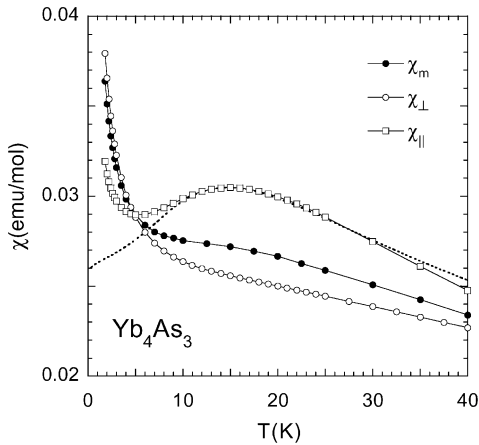


Fig. 14. Temperature dependence of the susceptibility of Yb_4As_3 along (χ_{\parallel}) and perpendicular (χ_{\perp}) to the trigonal axis as well as that of a polydomain sample (χ_m) [51]. The dotted line shows a fit to the χ_{\parallel} data including the uniform susceptibility of the $S = \frac{1}{2}$ antiferromagnetic Heisenberg chain χ_{1D} [52] with exchange coupling $J = 26\text{ K}$ [53] and a constant van Vleck term χ_{vV} .

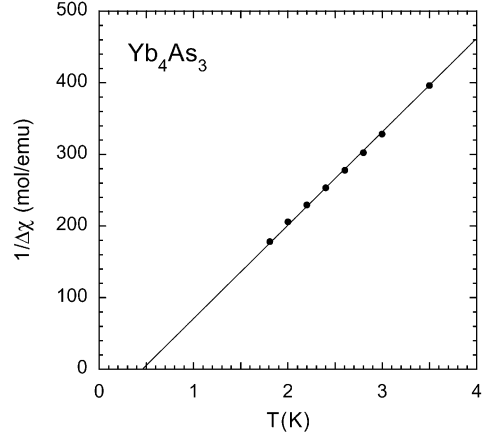


Fig. 15. Inverse of the static magnetic susceptibility $\Delta\chi_{\parallel} = \chi_{\parallel} - (\chi_{1D} + \chi_{vV})$ (see dotted line in Fig. 14) vs. T [8].

causes a $1/T$ divergence of the susceptibility [43]. Since no staggered field is induced for magnetic fields applied parallel to the trigonal axis, i.e., parallel to the spin chains, the upturn of $\chi_{\parallel}(T)$ below 7 K, i.e. the deviation from the dotted line in Fig. 14, cannot be explained within the staggered-field SG model.

Fig. 15 shows the inverse of this deviation $\Delta\chi_{\parallel} = \chi_{\parallel} - (\chi_{1D} + \chi_{vV})$ as a function of temperature. $\Delta\chi_{\parallel}$ follows a Curie–Weiss law $\Delta\chi_{\parallel} = C/(T - \Theta)$ with a positive Weiss temperature, Θ , indicating a dominating ferromagnetic interaction [8]. This is not related to possible magnetic impurities. The upturn does not significantly increase with decreasing sample quality [8]. Since the charge ordering in Yb_4As_3 is not perfect one might relate $\Delta\chi_{\parallel}$ to a contribution of the “free spins” at the chain edges. Doping with Lu^{3+} -ions on the Yb^{3+} -sites in $(\text{Yb}_{1-x}\text{Lu}_x)_4\text{As}_3$, one can increase the number of edges of the one-dimensional chains. This leads to an additional Curie–Weiss contribution in the low-temperature susceptibility which is proportional to x [8]. This contribution, however, shows a negative Weiss temperature indicating an antiferromagnetic interaction between the “free spins” at the chain edges. Edge effects can, therefore, not explain the ferromagnetic Curie–Weiss term in $\chi_{\parallel}(T)$. We, therefore, believe that the upturn in $\chi_{\parallel}(T)$ is intrinsic to Yb_4As_3 and is caused by a weak ferromagnetic interchain coupling.

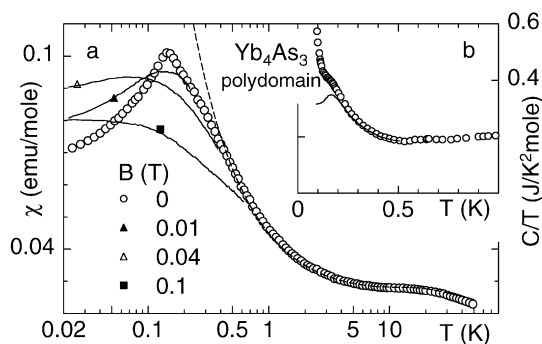


Fig. 16. Magnetic susceptibility as χ vs. T on a logarithmic scale (a) and specific heat as C/T vs. T (b), taken from Ref. [31], for polydomain Yb_4As_3 . The solid line in (b) shows the data after subtraction of nuclear contributions.

To investigate the susceptibility of Yb_4As_3 at sufficiently low temperatures, where the inter-chain-coupling effects become important, we used a low-frequency (15.9 Hz) ac technique and scaled the $\chi_{\text{ac}}(T)$ data in the temperature range $2 \text{ K} \leq T \leq 6 \text{ K}$ to $\chi(T) = M(T)/B$ results obtained by using a commercial SQUID magnetometer at $B = 0.01 \text{ T}$. As shown in Fig. 16a [54], for $T \geq 0.4 \text{ K}$, $\chi_{\text{ac}}(T)$ agrees well with the theoretical curve using the same parameters as in Ref. [43]. Below $T \approx 0.15 \text{ K}$, a cusp-like anomaly occurs which broadens substantially in $B = 0.01 \text{ T}$, shifts to lower temperature and vanishes for $B > 0.04 \text{ T}$. This temperature range is somewhat higher than $T = 0.045 \text{ K}$, which is the upper boundary for magnetic ordering with moments larger than $0.15\mu_B$ as inferred from ^{170}Yb Mössbauer spectroscopy [9].

On the other hand, a broad peak in the low- T specific heat measured [30,31] on a polydomain sample around 0.17 K (Fig. 16, part (b)) was attributed to spin-glass-type effects as well. (i) The upturn in $C(T)/T$ measured at fixed field can be well described by a $1/T^3$ dependence. This describes the high- T tail of a nuclear Schottky anomaly involving an average “internal field” $B_{\text{av}} \approx 56 \text{ T}$ which is forming in the spin-glass state and is acting on the nuclear spins of the ^{171}Yb , ^{173}Yb , and ^{75}As isotopes [30]. In accordance with neutron-scattering data [49], the effective magnetic moment of the Yb^{3+} -ions amounts to $\mu_{\text{eff}} \approx 0.5\mu_B$.

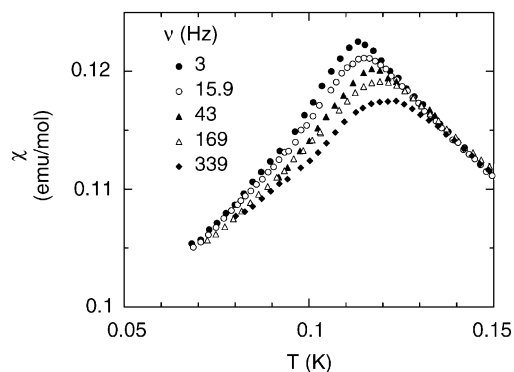


Fig. 17. Magnetic ac-susceptibility ($B_{\text{ac}} = 10 \text{ mT}$) at $B_{\text{dc}} = 0$ measured for different frequencies ν .

(ii) The field dependence of the peak at $T = 0.17 \text{ K}$ which is obtained after subtracting the “upturn” from the raw data in Fig. 16b is typical [30,31] for spin glasses [56].

Further evidence of spin-glass freezing arises from subsequent $\chi_{\text{ac}}(T, \nu)$ measurements on a different (polydomain) single crystal at various frequencies ν [55]. From the data shown in Fig. 17, the frequency shift $\Delta\nu = \Delta T_f / (\Delta \log(2\pi\nu) T_f)$ of the freezing temperature T_f per decade in ν , is estimated to be $\Delta\nu = 0.03 \pm 0.005$. This value is just between typical values for the frequency shift in metallic spin glasses, e.g., CuMn : $\Delta\nu = 0.005$, and insulating ones, e.g. $(\text{EuSr})\text{S}$: $\Delta\nu = 0.06$ [56].

Since each $S = \frac{1}{2}$ chain has six neighboring $S = \frac{1}{2}$ chains (see Fig. 1), the *antiferromagnetic* intra-chain coupling together with the *ferromagnetic* interchain coupling leads to strong frustration. Taken together with the disorder that is present on the Yb^{3+} -chains as inferred from the thermal-conductivity measurements described above, the spin-glass effects can be understood quite naturally.

To investigate whether domain disorder affects the spin-glass behavior we studied the anisotropy of $\chi_{\text{ac}}(T)$ by using a small CuBe uniaxial pressure cell that fits in both the commercial SQUID magnetometer as well as in our low- T χ_{ac} coil system. Our preliminary result is that the low- T susceptibility for a monodomain Yb_4As_3 crystal measured parallel to the Yb^{3+} -chains $\chi_{\parallel}(0.1 \text{ K})$

equals that of about $0.6\chi_m(0.1\text{ K})$, where $\chi_m(0.1\text{ K})$ is the value found for a polydomain Yb_4As_3 crystal [55]. The spin-glass cusp is also present in $\chi_{\parallel}(T)$, and the freezing temperature is not changed. This provides evidence that disorder on a smaller scale than the domain disorder is the cause for the spin-glass effects in Yb_4As_3 .

6. Resistivity and magnetoresistivity

The electrical resistivity of Yb_4As_3 , $\rho(T)$, was reported to follow a T^2 law between 2 and 100 K with a large coefficient $A \approx 0.75\ \mu\Omega\text{ cm}/\text{K}^2$ that fulfills (within a factor of 2) the Kadowaki–Woods scaling [5] found for typical heavy-fermion metals. However, the low carrier concentration of only about 0.001 per formula unit [5] excludes the usual Kondo effect underlying the formation of heavy quasiparticles in metallic strongly correlated electron systems. Light [$m = (0.6\dots 0.8)m_0$ [57], m_0 : free-electron mass] As-4p holes dominate the electrical conductivity in Yb_4As_3 [5,57]. Another striking evidence against the Kondo scenario is obtained comparing the specific-heat with the resistivity data of the P- and Sb-doped compounds shown in Fig. 6: The low-temperature resistivity in these crystals varies by four orders of magnitude and changes to an activated behavior in the P-doped case, while the specific-heat γ value is roughly the same. As discussed below, the origin of the heavy-fermion-like behavior of the resistivity of Yb_4As_3 is not yet clear.

All experiments were carried out on high-quality single crystals prepared as described in Ref. [5] with the current and magnetic field aligned along one of the cubic $\langle 111 \rangle$ axes. Electrical contacts were made by point welding 50 μm Au wires on the polished crystal surface.

As shown in Fig. 18, part (a), the resistivity follows an AT^2 temperature dependence with $A = 3.4\ \mu\Omega\text{ cm}/\text{K}^2$ down to 4 K. At lower temperatures, $\rho(T)$ deviates from the T^2 dependence, passes a minimum at 2 K followed by an 0.15% increase which saturates below 0.1 K, see Fig. 18b. Compared to the early measurement by Ochiai et al. [5], our recent experiments reveal a roughly three times higher residual resistivity ρ_0 and a

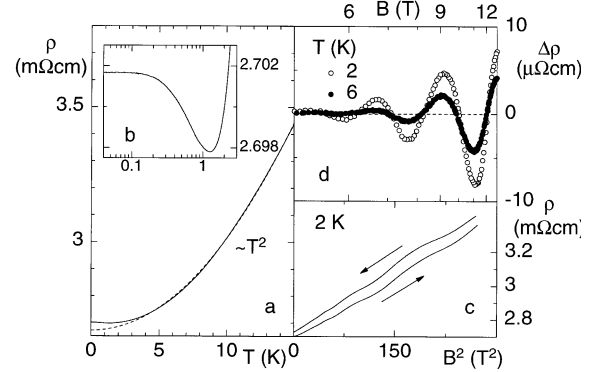


Fig. 18. Electrical resistivity for polydomain Yb_4As_3 , plotted as ρ vs T (a), ρ vs $\log(T/\text{K})$ (b), and ρ vs B^2 (c). The dashed line in (a) represents a T^2 dependence, the arrows in (c) indicate the magnetic history of the data. The offset at maximum field is due to relaxation [55]. (d) Shubnikov–de Haas oscillations at two different temperatures.

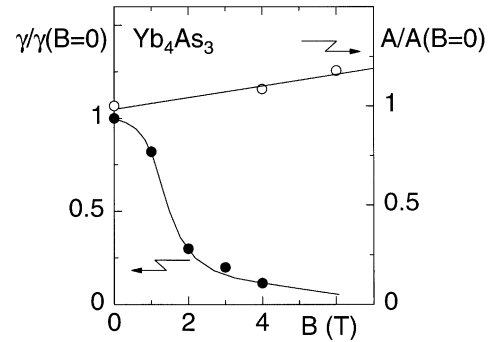


Fig. 19. Linear coefficient of low- T specific heat $\gamma = C/T$ [30,31] as well as the coefficient A of the $\rho(T) = \rho_0 + AT^2$ -behavior between 2 and 6 K [54], normalized to their values at $B = 0$. The lines are guides to the eyes.

more than two times larger Hall coefficient [55]. The mobility of the charge carriers remains virtually unchanged.

The large coefficient A remains almost unchanged in an applied magnetic field up to 18 T [54], while the specific-heat coefficient γ rapidly decreases due to the gap formation [30,31] (Fig. 19). This observation seems to be in conflict with the interpretation of a large A coefficient resulting from the scattering of light charge carriers off the magnon excitations [57,58].

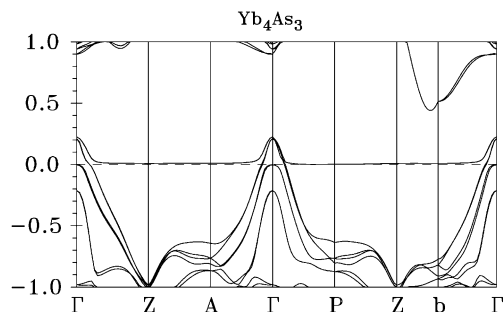


Fig. 20. Self-consistent LSDA+U energy band structure of Yb_4As_3 for energies close to the Fermi level [57].

For heavy-fermion metals, like CeCu_6 , UPt_3 , CeRu_2Si_2 , and CeCu_2Si_2 , both light ($m^* \sim m_e$) and heavy ($m^* \sim 100m_e$) quasiparticles were found in de Haas–van Alphen experiments [59–62]. In a heavy Fermi liquid, it is the scattering of the light and mobile charge carriers by the heavier ones that gives rise to the large A coefficient [63]. We propose that in Yb_4As_3 it is the scattering of the light and mobile As-4p holes by the heavy Yb-4f electrons [57] that leads to the large A coefficient in the resistivity.

Fig. 20 shows the LSDA+U energy band structure of Yb_4As_3 for energies close to the Fermi level calculated by Antonov et al. [57]. The U value in this case was adjusted to $U_{\text{eff}}^{3+} = 9.6$ eV, and the f shell of the Yb^{2+} -ions was treated as a core shell. Due to the gap between the As 4p and the Yb 5d bands, an extremely narrow marginally occupied Yb^{3+} 4f hole band is pinned to the top of the As 4p valence band via the charge balance between Yb and As. This charge balance also pins the Fermi level close to the bottom of the 4f hole band, leading to the extremely low carrier concentration in Yb_4As_3 . The Fermi surface therefore consists of (1) a hole pocket of As 4p states centered on the Γ point with an effective mass of $m_{\text{eff}} = (0.6 \dots 0.8)m_0$, and (2) an electron pocket of Yb 4f states with a heavy mass centered on the Γ -P symmetry line (Fig. 21).

The band structure, and thus the scattering mechanism described above, should not be affected by magnetic fields of the order of 10 T. Therefore, the A coefficient also remains almost constant and does not show any signatures of the

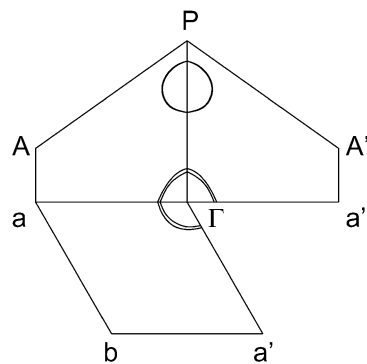


Fig. 21. Cross sections of the calculated Fermi surface of Yb_4As_3 [57]. The Fermi surface consists of a hole pocket of As 4p states centered on the Γ point, and an electron pocket of Yb 4f states on the Γ -P symmetry line.

field-induced gap in the spin excitation spectrum found in the specific heat [31].

The isothermal resistivity (Fig. 18c) roughly follows a B^2 -behavior which is typical for compensated semimetals. Shubnikov–de Haas oscillations with a frequency of 25 T, also found by Ochiai et al. [64], are clearly seen in the magnetic-field interval $B = 4.5 \dots 12$ T (Fig. 18d). For larger fields, additional oscillations are visible [54,55] which might be related to spin splitting because, due to the extremely low carrier concentration, the system is very close to the quantum limit.

Both the hole and the electron sheets of the Fermi surface are almost spherical. Since the mobility of the heavy 4f electrons is assumed to be almost negligible in comparison to the mobility of the As 4p holes, the Shubnikov–de Haas oscillations should arise from the most isotropic part of the As 4p bands. From the charge-carrier concentration $n \approx 3 \times 10^{18} \text{ cm}^{-3}$ determined from our new Hall effect measurements [55], assuming a single spherical spin-orbit split pair of As 4p hole orbits, a Shubnikov–de Haas frequency of 44 T is expected. In contrast, the observed frequency of 25 T leads to a carrier concentration of $n \approx 7 \times 10^{17} \text{ cm}^{-3}$ only. The reason for this discrepancy is yet unclear and deserves further investigations.

From the T -dependence of the oscillation (Fig. 18d) we estimate an effective carrier mass of $m_{\text{eff}} = (0.275 \pm 0.005)m_0$ [55]. Our results confirm

the existence of a low-density system of mobile As p holes that determines $\rho(T)$.

7. Conclusion and outlook

We have presented an interpretation of the exceptional thermodynamic, magnetic and transport properties of Yb_4As_3 and its Sb and P substituted crystals. These mixed-valent pnictides exhibit a charge ordering of Yb^{2+} and Yb^{3+} driven by intersite Coulomb interactions and a deformation potential coupling to the lattice. This transition is of central importance for its low-temperature physical properties. The observation of spin excitations which can be described by the des Cloiseaux–Pearson two-spinon continuum as evident from the q -dependence and the typical one-dimensional asymmetry of the spectral shape [35], the compelling evidence for soliton excitations in a transverse field and the presence of the large γ value even for P-doped insulating crystals proves beyond any reasonable doubt that Yb_4As_3 is a quasi-one-dimensional antiferromagnetic spin-chain system. Furthermore, the observation of a very low spin-glass freezing temperature proves that the interchain coupling is indeed very weak due to the large distance between the parallel chains.

It must be kept in mind, however, that Yb_4As_3 is not an ideal one-dimensional Heisenberg antiferromagnet because of its semimetallic character. This has interesting consequences with respect to transport behavior which suggest a two-band model of current-carrying 4p holes and heavy, almost localized, 4f states of the electron pocket that act as scattering centers, presumably leading to a field-independent T^2 coefficient in the resistivity. This mechanism still needs a more detailed theoretical investigation.

The same is true for the zero-field low-temperature thermal conductivity which appears also to be dominated by the spin excitations. In contrast to the electrical resistivity, here the scattering from static point defects seems to play an important role.

That the number of carriers can be reduced by doping with P is well understood from band-

structure calculations [57]. Eventually, pure Yb_4P_3 is an insulator and should be an ideal quasi-one-dimensional Heisenberg antiferromagnet below T_{co} . It still exhibits a large γ value, presumably determined by the one-dimensional spin excitations. It would be important to confirm this conjecture directly by determining their spectrum by inelastic neutron scattering as presented in Fig. 7 for the case of Yb_4As_3 .

8. Uncited Reference

[65]

Acknowledgements

We would like to thank Prof. P. Fulde for long-standing fruitful cooperations in the field of strongly correlated electron systems. We also want to thank Prof. K. Ueda for various valuable discussions.

References

- [1] J. des Cloiseaux, J.J. Pearson, *Phys. Rev.* 128 (1962) 2131.
- [2] P. Fulde, *Ann. Phys.* 6 (1997) 178.
- [3] E.J.W. Verwey, P.W. Haaymann, *Physica* 8 (1941) 979.
- [4] A. Yaresko, V. Antonov, H. Eschrig, P. Thalmeier, P. Fulde, *Phys. Rev. B* 62 (2000) 15538.
- [5] A. Ochiai, T. Suzuki, T. Kasuya, *J. Phys. Soc. Japan* 59 (1990) 4129.
- [6] A. Ochiai, H. Aoki, T. Suzuki, *JJAP Series* 11 (1998) 117.
- [7] A. Ochiai, H. Aoki, T. Suzuki, R. Helfrich, F. Steglich, *Physica B* 230–232 (1997) 708.
- [8] H. Aoki, Ph.D. Thesis, Tohoku University, 2000, unpublished.
- [9] P. Bonville, A. Ochiai, T. Suzuki, E. Vincent, *J. Phys. I (France)* 4 (1994) 595.
- [10] S. Suga, S. Ogawa, H. Namatame, M. Taniguchi, A. Kakizaki, T. Ishii, A. Fujimori, S.-J. Oh, H. Kato, T. Miyahara, A. Ochiai, T. Suzuki, T. Kasuya, *J. Phys. Soc. Japan* 58 (1989) 4534.
- [11] A. Ochiai, E. Hotta, Y. Haga, T. Suzuki, O. Nakamura, *J. Magn. Magn. Matter* 140–144 (1995) 1249.
- [12] H. Aoki, A. Ochiai, T. Suzuki, R. Helfrich, F. Steglich, *Physica B* 230–232 (1997) 698.
- [13] R.J. Gambino, *J. Less-Common Met.* 12 (1967) 344.
- [14] G. Wortmann, E.V. Sampathkumaran, G. Kaindl, *J. Magn. Magn. Mater.* 54–57 (1986) 338.

- [15] A. Ochiai, T. Suzuki, T. Kasuya, *J. Magn. Magn. Mater.* 52 (1985) 13.
- [16] A. Ochiai, Ph.D. Thesis, Tohoku University, 1988, unpublished.
- [17] K. Neumaier, K. Andres, *Physica B & C* 108 (1981) 1343.
- [18] M. O'Keeffe, S. Andersson, *Acta Crystallogr. A* 33 (1977) 914.
- [19] K. Iwasa, M. Kohgi, N. Nakajima, R. Yoshitake, Y. Hisazaki, H. Osumi, K. Tajima, N. Wakabayashi, Y. Haga, A. Ochiai, T. Suzuki, A. Uesawa, *J. Magn. Magn. Mater.* 177–181 (1998) 393.
- [20] P. Fulde, B. Schmidt, P. Thalmeier, *Europhys. Lett.* 31 (1995) 323.
- [21] K. Takegahara, Y. Kaneta, *J. Phys. Soc. Japan* 60 (1991) 4009.
- [22] T. Goto, Y. Nemoto, A. Ochiai, T. Suzuki, *Phys. Rev. B* 59 (1999) 269.
- [23] J. Labbé, J. Friedel, *J. Phys. France* 27 (1966) 153.
- [24] M. Rams, K. Królas, K. Tomala, A. Ochiai, T. Suzuki, *Hyperfine Interactions* 97–98 (1996) 125.
- [25] M. Kohgi, K. Isawa, A. Ochiai, T. Suzuki, J.-M. Mignot, B. Gillon, A. Gukasov, J. Schweizer, K. Kakurai, M. Nishi, A. Dönni, T. Osakabe, *Physica B* 230–232 (1997) 638.
- [26] K. Iwasa, M. Kohgi, A. Gukasov, J.-M. Mignot, A. Ochiai, H. Aoki, T. Suzuki, *Physica B* 281 & 282 (2000) 460.
- [27] S. Suga, A. Ochiai, T. Suzuki, H. Harada, A. Sekiyama, T. Matsushita, T. Iwasaki, A. Kimura, M. Tsunekawa, T. Muro, S. Ueda, H. Daimon, S. Imada, H. Namatame, M. Taniguchi, H. Ishii, T. Miyahara, T. Hanyu, A. Fujimori, *J. Phys. Soc. Japan* 67 (1998) 3552.
- [28] U. Staub, B.D. Patterson, C. Schulze-Briese, F. Fauth, M. Shi, L. Soderholm, G.B.M. Vaughan, A. Ochiai, *Europhys. Lett.* 53 (2001) 72.
- [29] O. Nakamura, N. Tomonaga, A. Ochiai, T. Suzuki, *Physica B* 171 (1991) 377.
- [30] R. Helfrich, Ph.D. Thesis, Darmstadt, 1996, unpublished.
- [31] R. Helfrich, M. Köppen, M. Lang, F. Steglich, A. Ochiai, *J. Magn. Magn. Mater.* 177–181 (1998) 309.
- [32] N. Read, D.M. Newns, *J. Phys. C* 16 (1983) 3273.
- [33] P. Lee, N. Nagaosa, *Phys. Rev. B* 46 (1992) 5621.
- [34] M. Kohgi, K. Isawa, J.-M. Mignot, N. Pyka, A. Ochiai, H. Aoki, T. Suzuki, *Physica B* 259–261 (1999) 269.
- [35] G. Müller, H. Beck, I.C. Bonner, *Phys. Rev. Lett.* 43 (1979) 75.
- [36] A.H. Bougourzi, M. Couture, M. Kacir, *Phys. Rev. B* 54 (1996) 12 669.
- [37] U. Ahlheim, Ph.D. Thesis, Darmstadt, 1991, unpublished.
- [38] U. Burkhardt, Y. Grin, H.G. von Schnering, Abstract PA 124, VIth European Conference on Solid State Chemistry, Zürich, 1997.
- [39] B. Schmidt, P. Thalmeier, P. Fulde, *Europhys. Lett.* 35 (1996) 109.
- [40] G. Uimin, Y. Kudasov, P. Fulde, A. Ovchinnikov, *Eur. Phys. J. B* 16 (2000) 241.
- [41] D.C. Dender, P.R. Hammar, D.N. Reich, C. Broholm, G. Aeppli, *Phys. Rev. Lett.* 79 (1997) 1750.
- [42] M. Oshikawa, I. Affleck, *Phys. Rev. Lett.* 79 (1997) 2883.
- [43] M. Oshikawa, K. Ueda, H. Aoki, A. Ochiai, M. Kohgi, *J. Phys. Soc. Japan* 68 (1999) 3181.
- [44] H. Shiba, K. Ueda, O. Sakai, *J. Phys. Soc. Japan* 69 (2000) 1493.
- [45] M. Köppen, M. Lang, R. Helfrich, F. Steglich, P. Thalmeier, B. Schmidt, B. Wand, D. Pankert, H. Benner, H. Aoki, A. Ochiai, *Phys. Rev. Lett.* 82 (1999) 4548.
- [46] H.J. Mikeska, M. Steiner, *Adv. Phys.* 40 (1991) 191.
- [47] F. Steglich, M. Köppen, P. Gegenwart, T. Cichorek, B. Wand, M. Lang, P. Thalmeier, B. Schmidt, *Acta Phys. Pol. A* 97 (2000) 91.
- [48] J.A.H.M. Buijs, W.J. de Jonge, *J. Phys. C* 15 (1982) 6631.
- [49] M. Kohgi, K. Iwasa, J.-M. Mignot, B. Fåk, P. Gegenwart, M. Lang, A. Ochiai, H. Aoki, *Phys. Rev. Lett.* 86 (2001) 2439.
- [50] K. Iwasa, M. Kohgi, A. Gukasov, J.-M. Mignot, N. Shibata, A. Ochiai, H. Aoki, T. Suzuki, *J. Magn. Magn. Mater.* (2001), in press.
- [51] H. Aoki, A. Ochiai, M. Oshikawa, K. Ueda, *Physica B* 281 & 282 (2000) 465.
- [52] S. Eggert, I. Affleck, M. Takahashi, *Phys. Rev. Lett.* 73 (1994) 332.
- [53] M. Kohgi, K. Iwasa, J.-M. Mignot, A. Ochiai, T. Suzuki, *Phys. Rev. B* 56 (1997) R 11 388.
- [54] P. Gegenwart, T. Cichorek, J. Custers, M. Lang, H. Aoki, A. Ochiai, F. Steglich, *J. Magn. Magn. Mater.* (2001), in press.
- [55] P. Gegenwart et al., in preparation.
- [56] J.A. Mydosh, *Spin glasses: an experimental introduction*, Taylor & Francis, London, 1993.
- [57] V.N. Antonov, A.N. Yaresko, A.Ya. Perlov, P. Thalmeier, P. Fulde, P.M. Oppeneer, H. Eschrig, *Phys. Rev. B* 58 (1998) 975.
- [58] A.A. Zvyagin, *Phys. Rev. B* 62 (2000) 12 175.
- [59] P.H.P. Reinders, M. Springford, P.T. Coleridge, R. Boulet, D. Ravot, *Phys. Rev. Lett.* 57 (1986) 1631.
- [60] L. Taillefer, G.G. Lonzarich, *Phys. Rev. Lett.* 60 (1988) 1570.
- [61] H. Aoki, S. Uji, A.K. Albessard, Y. Ōnuki, *Phys. Rev. Lett.* 71 (1993) 2110.
- [62] M. Hunt, P. Meeson, P.-A. Probst, P.H.P. Reinders, M. Springford, W. Assmus, W. Sun, *J. Phys. Condens. Matter* 2 (1990) 6859.
- [63] G. Zwircknagl, *Adv. Phys.* 41 (1992) 203.
- [64] A. Ochiai, H. Aoki, N. Kimura, T. Terashima, C. Terakura, Y. Shima, *Newsletter of Scientific Research on Priority Areas B* 1 (2000) 248.
- [65] H. Matsui, T. Yasuda, A. Ochiai, H. Harima, H. Aoki, T. Suzuki, N. Toyota, *Physica B* 246–247 (1998) 460.